INTERNATIONAL JOURNAL FOR NUMERICAL METHODS IN FLUIDS
Int. J. Numer. Meth. Fluids 2004; **45**:1025–1046 (DOI: 10.1002/fld.728)

Evaluation of an energy relaxation method for the simulation of unsteady, viscous, real gas flows

Emmanuel Bongiovanni[1], Alexandre Ern[2,*,†] and Nathalie Glinsky-Olivier[1]

[1]*CERMICS, INRIA, BP 93, 06902 Sophia-Antipolis Cedex, France*
[2]*CERMICS, Ecole Nationale des Ponts et Chaussées, 77455 Marne la Vallée Cedex 2, France*

SUMMARY

This study investigates a new energy relaxation method designed to capture the dynamics of unsteady, viscous, real gas flows governed by the compressible Navier–Stokes equations. We focus on real gas models accounting for inelastic molecular collisions and yielding temperature-dependent heat capacities. The relaxed Navier–Stokes equations are discretized using a mixed finite volume/finite element method and a high-order time integration scheme. The accuracy of the energy relaxation method is investigated on three test problems of increasing complexity: the advection of a periodic set of vortices, the interaction of a temperature spot with a weak shock, and finally, the interaction of a reflected shock with its trailing boundary layer in a shock tube. In all cases, the method is validated against benchmark solutions and the numerical errors resulting from both discretization and energy relaxation are assessed independently. Copyright © 2004 John Wiley & Sons, Ltd.

KEY WORDS: Navier–Stokes; real gas; computational fluid dynamics; energy relaxation method; vorticity production; shock boundary layer interaction

1. INTRODUCTION

Many engineering applications involve unsteady, viscous flows governed by the compressible Navier–Stokes equations. In these equations, the vector of conservative variables has components $(\rho, \rho U, E)$ where ρ is the density, U the velocity vector in the physical space $\mathbb{R}^d$, d the space dimension, $E = \frac{1}{2}\rho U^2 + \rho\varepsilon$ the total energy per unit volume, and ε the specific internal energy. It is well-known that the convective and diffusive fluxes in the compressible Navier–Stokes equations involve two additional quantities, namely the pressure p and the temperature T, and that the governing equations are closed upon expressing these latter quantities in terms of the conservative variables by means of a suitable thermodynamic model.

*Correspondence to: Alexandre Ern, CERMICS, Ecole Nationale des Ponts et Chaussées, 6 et 8 avenue Blaise Pascal, 77455 Marne la Vallée Cedex 2, France.
†E-mail: ern@cermics.enpc.fr

Published online 4 May 2004

Received 24 February 2003
Revised 7 March 2004

The simplest thermodynamic model is the thermically perfect and calorifically perfect gas model (TPCP, also termed the polytropic ideal gas model) in which

$$p = (\gamma - 1)\rho\varepsilon = \rho RT \tag{1}$$

where $\gamma > 1$ and R are given constants. The TPCP gas model has been often considered in applications and several finite volume solvers dedicated to TPCP gas flows have been developed over the last decade. Because of the substantial development efforts devoted to these codes, most of them may be considered as fairly robust and computationally effective.

However, the TPCP gas model is only reasonable for monatomic gases. For polyatomic gases, the thermodynamic model must account for inelastic energy transfer in microscopic collisions. This effect becomes more pronounced at high temperatures and leads to a temperature dependency of the heat capacity. A more appropriate thermodynamic model is then the thermically perfect gas model (TP) for which the ideal gas law $p = \rho RT$ still holds, but the specific internal energy ε is a non-linear function of the temperature. Further complexities arise in high pressure gas flows since the pressure becomes a non-linear function of the density. A gas requiring a more complex thermodynamic model than the TPCP one will be termed a real gas. In this work, we shall be concerned with polyatomic, viscous gas flows with pressures and temperatures up to 10^7 Pa and 2000 K, respectively. As discussed in Reference [1], for most gases at such conditions, the TP gas model remains appropriate and this model is indeed often considered in applications involving polyatomic gas flows over a relatively wide pressure and temperature range. We shall therefore keep this approach in the present work. One interesting feature of the TP gas model is that it may be recovered along with the compressible Navier–Stokes equations from the kinetic theory of dilute polyatomic gases and the first-order Enskog–Chapman expansion.

From a numerical viewpoint, the main difficulty when dealing with real gas flows is that it is not straightforward to extend finite volume codes designed for TPCP flows since the Riemann solver directly relies on the TPCP gas model. Previous work aimed at extending exact or approximate Riemann solvers includes References [2–4]. Most of these extensions are tailored to handle specific applications and often involve sizeable computational overheads with respect to the TPCP case. Alternatively, an appealing approach to tackle real gas flows is to consider a relaxation method. Such methods have been introduced for the numerical simulation of hyperbolic systems in References [5, 6]. Recently, an energy relaxation method has been introduced for the Euler equations [7] and then extended to the Navier–Stokes equations [8]. In this method, one considers a fictitious TPCP gas with specific internal energy ε_1. For inviscid flows, the relaxed equations consist of the Euler equations for the fictitious gas coupled with a transport equation for the perturbation $\varepsilon_2 = \varepsilon - \varepsilon_1$. For viscous flows, a suitable decomposition of the diffusion fluxes must also be specified [8]. The relaxation method presents several attractive features. Owing to its consistency property, the Euler or Navier–Stokes equations for the real gas are recovered in the limit of infinite relaxation. Furthermore, under some sub-characteristic conditions which will be restated hereafter, the relaxation method satisfies a stability property in the sense that the sign of a suitable entropy production during relaxation is controlled. From a practical viewpoint, the key advantage of the energy relaxation method is that TPCP Navier–Stokes codes may be used with very little modifications to simulate real gas flows.

This work's principal aim is to validate numerically the energy relaxation method derived theoretically in Reference [8] for Navier–Stokes flows. We investigate three test cases for

which highly accurate benchmark solutions are available [9, 10]. The first one, dealing with the advection of a Taylor vortex in a periodic flow, is an elementary test case in which the temperature is uniform. It provides a first assessment of dissipative errors. The second one concerns the interaction between a temperature spot and a weak shock. It enlightens the capability of the energy relaxation method to provide an accurate splitting of the diffusive fluxes in non-isothermal flows and also to capture the mechanism of vorticity generation through the baroclinic torque. In this second test case, the non-linearities present in the thermodynamic model have a moderate impact on the flow dynamics. The last test case investigates the interaction between the boundary layer generated behind a strong shock propagating in a shock tube and the reflected wave produced once the shock has reached the end wall of the tube. This last test case is particularly challenging to validate the accuracy of the relaxation method because inelastic energy transfer has a strong impact on the flow dynamics. The benchmark solutions in References [9, 10] correspond to TPCP gas flows. We will therefore validate the relaxation method by first considering such gases and then real gases endowed with more general thermodynamic models. For this second step, we shall consider temperature-dependent heat capacities resulting either from polynomial fits of experimental values or from a non-linear model involving a vibrational temperature. Similar thermodynamic models have been considered in References [11, 12] for the numerical validation of an energy relaxation method applied to the Euler equations.

The key features of the energy relaxation method derived in Reference [8] for the Navier–Stokes equations are briefly restated in Section 2. Numerical methods are described in Section 3. Numerical results are discussed in Section 4. Conclusions are drawn in Section 5.

2. THE ENERGY RELAXATION METHOD

The compressible Navier–Stokes equations express the conservation of mass, momentum, and energy in the form

$$\partial_t W + \sum_{1 \leqslant i \leqslant d} \partial_i \mathscr{F}_i^{\mathrm{c}}(W) + \sum_{1 \leqslant i \leqslant d} \partial_i \mathscr{F}_i^{\mathrm{d}}(W) = 0 \tag{2}$$

where ∂_t and ∂_i denote, respectively, the partial derivative with respect to time and the ith spatial Cartesian co-ordinate, and $W = (\rho, \rho U, E)^{\mathrm{T}} \in \mathbb{R}^{d+2}$ is the vector of conservative variables. The convective (or Euler) fluxes $\mathscr{F}_i^{\mathrm{c}}(W)$ are given by

$$\mathscr{F}_i^{\mathrm{c}}(W) = (\rho u_i, (\rho u_i u_j + p\delta_{ij})_{1 \leqslant j \leqslant d}, (E + p)u_i)^{\mathrm{T}} \tag{3}$$

where δ_{ij} is the Kronecker symbol and $(u_1, \ldots, u_d)^{\mathrm{T}}$ the Cartesian co-ordinates of the velocity vector U. The diffusive fluxes $\mathscr{F}_i^{\mathrm{d}}(W)$ may be expressed as

$$\mathscr{F}_i^{\mathrm{d}}(W) = \left(0, (\pi_{ij})_{1 \leqslant j \leqslant d}, q_i + \sum_{1 \leqslant j \leqslant d} \pi_{ij} u_j\right)^{\mathrm{T}} \tag{4}$$

where $\pi = (\pi_{ij})_{1 \leqslant i,j \leqslant d}$ is the momentum flux tensor ($-\pi$ is the viscous stress tensor) given by

$$\pi = -\eta(\nabla U + \nabla U^{\mathrm{T}}) + \tfrac{2}{3}\eta(\nabla \cdot U)I \tag{5}$$

I being the identity matrix and $\nabla = (\partial_1, \ldots, \partial_d)^{\mathrm{T}}$ the gradient operator. Furthermore, $q = (q_i)_{1 \leqslant i \leqslant d}$ is the heat flux vector given by

$$q = -\kappa \nabla T \tag{6}$$

The shear viscosity η and the thermal conductivity κ are positive, and for the sake of simplicity, we shall assume that these quantities are constant.

The energy relaxation method derived in Reference [8] is valid within a rather general thermodynamic framework which is briefly restated here. Letting $\tau = 1/\rho$ be the dilatation and $\varepsilon = \tau E - U^2/2$ be the specific internal energy, we assume that there exists a function $\sigma := \sigma(\tau, \varepsilon)$ called the specific (mathematical) entropy, which is strictly decreasing and strictly convex in the variables (τ, ε). The pressure and the temperature are then expressed as functions of (τ, ε) via Gibbs relations

$$T(\tau, \varepsilon) = -\frac{1}{\partial_{\varepsilon,\tau}\sigma(\tau, \varepsilon)}, \quad p(\tau, \varepsilon) = \frac{\partial_{\tau,\varepsilon}\sigma(\tau, \varepsilon)}{\partial_{\varepsilon,\tau}\sigma(\tau, \varepsilon)} \tag{7}$$

with obvious notation for the partial derivatives. For any fixed $\tau > 0$, we assume that the pressure $p := p(\tau, \varepsilon)$ is strictly increasing in ε with $p(\tau, 0) = 0$ and $p(\tau, \infty) = \infty$. The function $\varepsilon \mapsto p(\tau, \varepsilon)$ may then be inverted over $(0, \infty)$. This assumption obviously holds for TP gases.

For TPCP gases, the specific entropy is given, up to an additive constant, by

$$\sigma(\tau, \varepsilon) = c_v \log(\tau^{\gamma - 1}\varepsilon) \tag{8}$$

where $c_v = R/(\gamma - 1)$ is the constant volume specific heat capacity. For TP gases, the specific internal energy is a non-linear function of the temperature and therefore, the heat capacity $c_v(T) = \varepsilon'(T)$ depends on the temperature. The specific entropy is then given, up to an additive constant, by

$$\sigma(\tau, \varepsilon) = \int^{T(\varepsilon)} \frac{c_v(t)}{t}\, \mathrm{d}t + R \log \tau \tag{9}$$

We also introduce the adiabatic exponent $\gamma(T) = 1 + R/c_v(T)$. For polyatomic gases, one has $\gamma(T) \in (1, 1.4]$, whereas for monatomic gases, the adiabatic exponent is independent of the temperature and equal to $\frac{5}{3}$.

In order to derive the relaxed Navier–Stokes equations, consider a fictitious gas with the simple entropy $\sigma_1 := \sigma_1(\tau, \varepsilon_1)$ whence we deduce using Gibbs relations the simple pressure and temperature laws $p_1 := p_1(\tau, \varepsilon_1)$ and $T_1 := T_1(\tau, \varepsilon_1)$. For all practical purposes, the fictitious gas is TPCP and we denote by γ_1 its (constant) adiabatic exponent. We assume that γ_1 satisfies the subcharacteristic conditions [7]

$$\begin{aligned} \gamma_1 &> \sup_{\tau,\varepsilon} \tau(\partial_{\varepsilon,\tau} p(\tau, \varepsilon) - \partial_{\tau,\varepsilon} \log p(\tau, \varepsilon)) \\ \gamma_1 &> \sup_{\tau,\varepsilon} \tau \partial_{\varepsilon,\tau} p(\tau, \varepsilon) + 1 \end{aligned} \tag{10}$$

In the case where the real gas is TP, these conditions simply reduce to

$$\gamma_1 > \sup_T \gamma(T) \tag{11}$$

One easily shows that there exists a function F defined over $\mathbb{R}_+^2$ and such that for $(\tau,\varepsilon_1)\in\mathbb{R}_+^2$, we have $p(\tau,\varepsilon_1+F(\tau,\varepsilon_1))=p_1(\tau,\varepsilon_1)$ [7]. Furthermore, there exist two functions, $\mathscr{T}$ and $\mathscr{E}_1$, of (σ_1,ε_2) such that $\mathscr{T}(\sigma_1,\varepsilon_2)=\tau$ and $\mathscr{E}_1(\sigma_1,\varepsilon_2)=\varepsilon_1$ if $\sigma_1=\sigma_1(\tau,\varepsilon_1)$ and $\varepsilon_2=F(\tau,\varepsilon_1)$. It is then possible to introduce the global entropy functional

$$\Sigma(\tau,\varepsilon_1,\varepsilon_2)=\sigma(\mathscr{T}(\sigma_1,\varepsilon_2),\mathscr{E}_1(\sigma_1,\varepsilon_2)+\varepsilon_2) \tag{12}$$

which is compatible with the specific entropy of the real gas at equilibrium, i.e. if $\varepsilon_2=F(\tau,\varepsilon_1)$, we have $\Sigma(\tau,\varepsilon_1,\varepsilon_2)=\sigma(\tau,\varepsilon_1+\varepsilon_2)$. Finally, letting $\alpha:=\alpha(\tau,\varepsilon_1)$ be an arbitrary function of (τ,ε_1) taking its values in $[0,1]$, we introduce the following functions of $(\tau,\varepsilon_1,\varepsilon_2)$:

$$\begin{aligned}\Theta(\tau,\varepsilon_1,\varepsilon_2)&=-((1-\alpha)\partial_{\sigma_1,\varepsilon_2}\Sigma(\sigma_1,\varepsilon_2)\partial_{\varepsilon_1,\tau}\sigma_1(\tau,\varepsilon_1)+\alpha\partial_{\varepsilon_2,\sigma_1}\Sigma(\sigma_1,\varepsilon_2))^{-1}\\ \beta(\tau,\varepsilon_1,\varepsilon_2)&=\alpha+(1-\alpha)\frac{\partial_{\varepsilon_1,\tau}\sigma_1(\tau,\varepsilon_1)}{\partial_{\varepsilon_1,\tau}\sigma_1(\mathscr{T}(\sigma_1,\varepsilon_2),\mathscr{E}_1(\sigma_1,\varepsilon_2))}\end{aligned} \tag{13}$$

with α and σ_1 evaluated at (τ,ε_1). Note that Θ has dimensions of a temperature whereas β is dimensionless.

Using the above notation, the relaxed Navier–Stokes equations may be written as [8]

$$\partial_t\mathscr{W}+\sum_{1\leqslant i\leqslant d}\partial_i\mathscr{F}_i^{c*}(\mathscr{W})+\sum_{1\leqslant i\leqslant d}\partial_i\mathscr{F}_i^{d*}(\mathscr{W})+\Omega(\mathscr{W})=0 \tag{14}$$

where $\mathscr{W}=(\rho,\rho U,E_1,\rho\varepsilon_2)^{\mathrm{T}}\in\mathbb{R}^{d+3}$ is the vector of conservative variables. The convective fluxes $\mathscr{F}_i^{c*}(\mathscr{W})$ are given by

$$\mathscr{F}_i^{c*}(\mathscr{W})=(\rho u_i,(\rho u_iu_j+p_1\delta_{ij})_{1\leqslant j\leqslant d},(E+p_1)u_i,\rho u_i\varepsilon_2)^{\mathrm{T}} \tag{15}$$

with $p_1:=p_1(\tau,\varepsilon_1)$ and $\rho\varepsilon_1=E_1-\frac{1}{2}\rho U^2$. The diffusive fluxes $\mathscr{F}_i^{d*}(\mathscr{W})$ may be expressed as

$$\mathscr{F}_i^{d*}(\mathscr{W})=\left(0,(\pi_{ij})_{1\leqslant j\leqslant d},q_{1,i}+\sum_{1\leqslant j\leqslant d}\pi_{ij}u_j,0\right)^{\mathrm{T}} \tag{16}$$

where $q_1=(q_{1,i})_{1\leqslant i\leqslant d}$ is the heat flux vector associated with the fictitious gas, i.e. $q_1=-\kappa\nabla T_1$. Finally, the source term is given by

$$\Omega(\mathscr{W})=(0,(0)_{1\leqslant i\leqslant d},\Omega_{\varepsilon_1},-\Omega_{\varepsilon_1}-\Omega_{\varepsilon_2})^{\mathrm{T}} \tag{17}$$

with

$$\begin{aligned}\Omega_{\varepsilon_1}&=\alpha(\pi:\nabla U+\nabla\cdot q_1)+\lambda\rho(\varepsilon_2-F(\tau,\varepsilon_1))\\ \Omega_{\varepsilon_2}&=\beta\nabla\cdot q_2\end{aligned} \tag{18}$$

Here, $\lambda\in\mathbb{R}$ is the relaxation parameter and the heat flux perturbation q_2 is defined as

$$q_2=\mathscr{Q}-q_1\quad\text{with}\quad\mathscr{Q}=-\kappa\nabla\Theta \tag{19}$$

The relaxed Navier–Stokes equations (14) thus consist of the Navier–Stokes equations for the fictitious gas (up to a weighting coefficient in the source term of the energy equation) coupled with a transport equation for the energy perturbation ε_2. The parameter α acts as a weighting parameter to distribute the diffusive contribution $\pi:\nabla U+\nabla\cdot q_1$ between the

balance equations for E_1 and $\rho\varepsilon_2$. System (14) is endowed with important properties proven in Reference [8]:

- *Consistency*: at equilibrium, i.e. in the limit $\lambda \to \infty$, the vector $W = (\rho, \rho U, E_1 + \rho\varepsilon_2)$ satisfies the Navier–Stokes system (2) with the pressure and temperature laws of the real gas;
- *Global stability*: assuming that $\mathscr{W}$ is smooth and that $(\varepsilon_1, \varepsilon_2) \in \mathbb{R}^2_+$, the volumetric entropy $S(\mathscr{W}) = \rho\Sigma(\sigma_1(\tau, \varepsilon_1), \varepsilon_2)$ satisfies for all λ the balance equation

$$\partial_t S(\mathscr{W}) + \nabla \cdot (US(\mathscr{W})) - \nabla \cdot \left(\frac{\mathscr{Q}}{\Theta}\right) = \lambda\omega_e + \frac{\pi : \nabla U}{\Theta} + \frac{\mathscr{Q} \cdot \nabla\Theta}{\Theta^2} \leqslant 0 \tag{20}$$

  the three terms in the r.h.s. being non-positive independently. The entropy source term ω_e represents the entropy production due to the relaxation process and is given explicitly in Reference [7]. Note that the entropy balance equation (20) indicates that the function Θ acts as a global temperature for the relaxed system (14);
- *Asymptotic stability around equilibrium states*: assuming that the real gas is TP and letting

$$\alpha := \alpha(\varepsilon_1) = \frac{\gamma_1 - \gamma(T_1)}{\gamma_1 - 1} \quad \text{with} \quad T_1 = \frac{R}{\gamma_1 - 1}\,\varepsilon_1 \tag{21}$$

  the vector $W = (\rho, \rho U, E_1 + \rho\varepsilon_2)$ is the solution, up to first order in $\frac{1}{\lambda}$, of the original Navier–Stokes equations (2) plus a dissipative perturbation. Details are given in Reference [8].

3. NUMERICAL METHODS

The relaxation method for the Navier–Stokes equations may be implemented using the following three-step procedure. A similar algorithm has been investigated numerically in References [11, 12] for the relaxed Euler equations.

- *Step 1*: given an approximate solution to the original Navier–Stokes equations (2) at a discrete time t^n, $W^n = (\rho^n, \rho^n U^n, E^n)$, one evaluates ε^n, τ^n, the pressure $p^n = p(\tau^n, \varepsilon^n)$, the internal energies $\varepsilon_1^n = p^n/((\gamma_1 - 1)\rho^n)$ and $\varepsilon_2^n = \varepsilon^n - \varepsilon_1^n$ and the temperature $T_1^n = (\gamma_1 - 1)\varepsilon_1^n/R$.
- *Step 2*: the relaxed Navier–Stokes equations (14) are integrated in time from t^n to t^{n+1} in the equilibrium limit ($\lambda \to \infty$). When the real gas is TP and the fictitious one TPCP, one easily checks that their temperatures coincide at equilibrium so that we may take $\beta = 1$ and $q_2 = 0$. We thus have $\Omega_{\varepsilon_2} = 0$ and the source term in (14) is given by

$$\Omega(\mathscr{W}) = (0, (0)_{1 \leqslant i \leqslant d}, \alpha(\pi : \nabla U + \nabla \cdot q_1), -\alpha(\pi : \nabla U + \nabla \cdot q_1))^{\mathrm{T}} \tag{22}$$

  The weighting coefficient α is evaluated using (21).
- *Step 3*: W^{n+1} is obtained by projection: $\rho^{n+1} = \rho^{n+1-}$, $(\rho U)^{n+1} = (\rho U)^{n+1-}$, $E^{n+1} = E_1^{n+1-} + (\rho\varepsilon_2)^{n+1-}$ where the superscript $^{n+1-}$ refers to the numerical values obtained at Step 2.

In Step 2, the relaxed Navier–Stokes equations can be discretized in space and time with any suitable numerical method. In this work, we consider a mixed finite volume/finite element method on unstructured, conforming triangulations. The convective fluxes and the source term

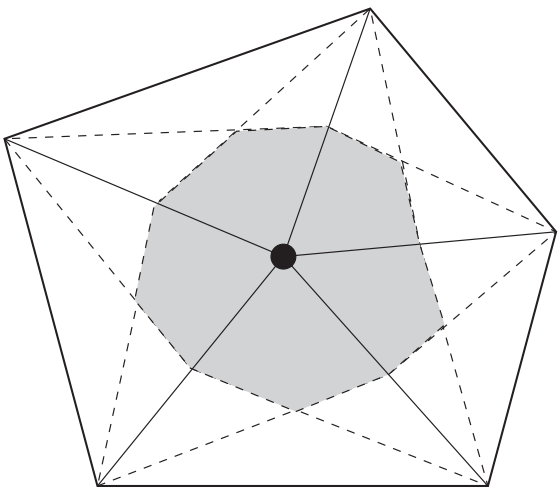

Figure 1. Finite element cell T_v centred on vertex v and consisting here of 5 mesh triangles; finite volume cell C_v (filled area).

are approximated using a finite volume method whereas the diffusive fluxes are approximated using P_1 Lagrange finite elements. Let v be a mesh vertex, T_v the set of triangles to which v belongs, N_v the finite element nodal function associated with vertex v (the continuous, piecewise affine function with support T_v and such that $N_v(v) = 1$) and let C_v the finite volume cell for vertex v (see Figure 1). The finite volume/finite element discretization of the relaxed Navier–Stokes equations may be written as

$$\frac{\mathrm{d}}{\mathrm{d}t}\int_{C_v} \mathscr{W} + \int_{\partial C_v} \sum_{1\leqslant i\leqslant d} \mathscr{F}_i^{\mathrm{c}*}(\mathscr{W})n_i - \int_{T_v} \sum_{1\leqslant i\leqslant d} \mathscr{F}_i^{\mathrm{d}*}(\mathscr{W})\partial_i N_v + \int_{C_v} \Omega(\mathscr{W}) = 0 \tag{23}$$

up to diffusive flux boundary contributions.

The convective fluxes along the interface ∂C_v are evaluated using a Roe scheme of order 3 owing to a combination of the MUSCL method and a β-scheme with $\beta = \frac{1}{2}$ or $\frac{1}{3}$ [13]. At a cell interface between two vertices i and j, the Roe scheme is applied to high-order interpolations W_{ij} and W_{ji} of W on both sides of the interface given by

$$W_{ij} = W_i + \tfrac{1}{2}(1-2\beta)(W_j - W_i) + \beta\nabla\overline{W}_i \cdot \vec{ij}$$

where $\nabla\overline{W}_i$ is the nodal-average gradient of W at vertex i. For the third test case presented below, a recent limiter designed for the Euler equations to yield third- and fourth-order accuracy in conjunction with the β-scheme and the MUSCL method has been implemented [14]. Set $\nabla W_{ij}^{\mathrm{up}} \cdot \vec{ij} = 2\nabla\overline{W}_i \cdot \vec{ij} - (W_j - W_i)$ and $\nabla W_{ji}^{\mathrm{up}} \cdot \vec{ji} = 2\nabla\overline{W}_j \cdot \vec{ji} - (W_i - W_j)$ and define the ratios

$$R_i = \frac{W_j - W_i}{\nabla W_{ij}^{\mathrm{up}} \cdot \vec{ij}} \quad \text{and} \quad R_j = \frac{W_{ji}^{\mathrm{up}} \cdot \vec{ji}}{W_i - W_j}$$

The third-order upwind scheme can be written as $W_{ij} = W_i + \frac{1}{2}\psi(R_i)\nabla W_{ij}^{\text{up}} \cdot \vec{ij}$ where the limiter function is given by $\psi(R) = (1/3 + 2R/3)\backslash\psi(R)$ with

$$\varphi(r) = \begin{cases} 0 & \text{if } r \leqslant 0 \\ \dfrac{3r^4 - 7r^3 + 3r^2 + 3r}{2} & \text{if } 0 \leqslant r \leqslant 1 \\ \dfrac{3r^2 - 6r + 19}{r^3 - 3r + 18} & \text{if } 1 \leqslant r \end{cases}$$

We also consider a fourth-order centred scheme in which $W_{ij} = W_i + \frac{1}{2}\psi(R_i, R_j)(W_j - W_i)$ where the limiter function $\psi(R,S) = R\,\varphi(R) + (\beta/2)\psi_1(R)\psi_2(S)$ depends on the three functions φ, ψ_1, and ψ_2 given by

$$\varphi(r) = \psi_1(r) = \psi_2(r) = 0 \quad \text{if } r \leqslant 0$$

$$\varphi(r) = -3r^5 + 11r^4 - 14r^3 + 6r^2 + 3, \quad \psi_1(r) = \psi_2(r) = \frac{r^3}{r^3 + (1-r)^3} \quad \text{if } 0 \leqslant r \leqslant 1$$

$$\varphi(r) = \psi_2(r) = 1, \quad \psi_1(r) = \frac{1}{1 + (r-1)^3} \quad \text{if } 1 \leqslant r$$

The Jacobian matrices of the convective fluxes considered in the Riemann solver are matrices of size $d + 3$. These matrices are straightforward extensions of the ones obtained without relaxation (and of order $d + 2$) and are independent of the pressure and temperature laws retained in the real gas model. The Jacobian matrices and the associated transformation matrices are detailed for two-dimensional flows in Reference [8]. An alternative approach is to uncouple the convective fluxes for the energy perturbation ε_2 from the convective fluxes for the fictitious gas. Indeed, ε_2 is simply convected by the fictitious gas flow velocity U and its convective flux may be approximated using the numerical scheme described in Reference [15] and designed to preserve mass fraction positivity in reactive flow computations. We have compared numerically both approaches on inviscid shock tube calculations and on vortex advection by viscous flows without observing any significant difference. The numerical results presented below are based on the first strategy.

Time integration is based on a fourth-order Runge–Kutta scheme. Time steps are evaluated using a CFL condition extended to the compressible Navier–Stokes equations and depending on the Reynolds and Prandtl numbers [16]. Unless stated otherwise, a CFL value of 1.5 has been used in the computations discussed below. Boundary conditions arising in our test problems are either of inflow/outflow type or of periodic type. The former are treated using a Steger–Warming scheme [17]. The latter are implemented upon reconstructing the whole finite volume cell across the boundary.

4. RESULTS AND DISCUSSION

In this section, we discuss our numerical results for the three test problems: the advection of a periodic set of vortices, the interaction between a temperature spot and a weak shock,

and the interaction between a reflected shock and the incident boundary layer in a shock tube. In each case, we first assess the accuracy of our numerical methods by comparing the results predicted by our TPCP Navier–Stokes code with benchmark solutions [9, 10]. We then investigate the accuracy of the energy relaxation method. All the results reported hereafter as well as the benchmark solutions correspond to two-dimensional flow simulations.

4.1. Advection of a periodic set of vortices

The initial condition consists of a periodic set of Taylor vortices superimposed to a uniform flow. The carrier gas is air at standard thermodynamic conditions: $p_0 = 103,320$ Pa, $T_0 = 300$ K and $\rho_0 = 1.2\ \mathrm{kg/m^{-3}}$. Since this test problem is practically isothermal, air is assumed to be TPCP with $\gamma = 1.4$. The advection velocity is initially $u_0 = 277.75$ m/s, corresponding to a Mach number of 0.8. The Taylor vortices are initially centred at the vertices of a two-dimensional, uniform lattice with step L along both Cartesian co-ordinates. The reference length scale is set to $L = 1$ m. The shear viscosity and the thermal conductivity are evaluated from a Reynolds number of 10^4 and a Prandtl number of 0.7. The computational domain is the unit two-dimensional square with periodic boundary conditions imposed on its four edges. Initially, the vortex is centred at point $(\frac{1}{2}, \frac{1}{2})$ and has a tangential velocity given in non-dimensional form by

$$u_\theta(r) = c_1 r \mathrm{e}^{-c_2 r^2} \tag{24}$$

with $r^2 = (x_1 - \frac{1}{2})^2 + (x_2 - \frac{1}{2})^2$, $c_1 = (u_v/r_v)\mathrm{e}^{1/2}$, $c_2 = 1/(2r_v^2)$, $u_v = 0.3$, and $r_v = 0.075$.

We first assess the basic dissipative errors of our numerical schemes in the absence of relaxation. We investigate two β-schemes ($\beta = \frac{1}{2}$ and $\frac{1}{3}$) and two triangulations. Both were obtained from a uniform, quadrangular mesh by splitting the cells along alternating diagonals. The coarse triangulation (mesh M1) contains 101×101 nodes and the fine one (mesh M2) contains 201×201 nodes. The reference solution has been obtained in Reference [9] using a third-order accurate TVD Runge–Kutta method for time integration and a sixth-order accurate Hermitian scheme for spatial discretization on a uniform, quadrangular mesh with 200×200 nodes.

Figure 2 presents non-dimensional profiles for the vertical velocity and the pressure along the line $y = \frac{1}{2}$ at time $t_5 = 5L/u_0$, i.e. when the vortex has been advected five computational domains further downstream. As expected, errors on the pressure are larger than those on the velocity. Mesh refinement has a more sizeable effect on quenching dissipative errors than the β-scheme. Table I reports relative errors for the maximum vertical velocity and the minimum pressure in the computational domain at times $t_i = iL/u_0$ with $1 \leqslant i \leqslant 5$. Note that the minimum pressure is not monotone in time as also reported in Reference [9]. The overall convergence order with respect to the benchmark solution is seen to be larger than 2. In addition, on a given mesh, changing coefficient β from $\frac{1}{2}$ to $\frac{1}{3}$ yields a further reduction in the error up to a factor of 2.

We have also compared the influence of the type of triangulation on solution accuracy. In addition to the structured triangulation with alternate diagonal splitting of the quadrangular cells, we have considered a structured triangulation with uniform splitting of the cells and a fully unstructured Delaunay triangulation with 46 569 nodes. The latter yields slightly more accurate results than the structured mesh with alternate splitting which in turn, yields slightly more accurate results than the structured mesh with uniform splitting. For instance, relative

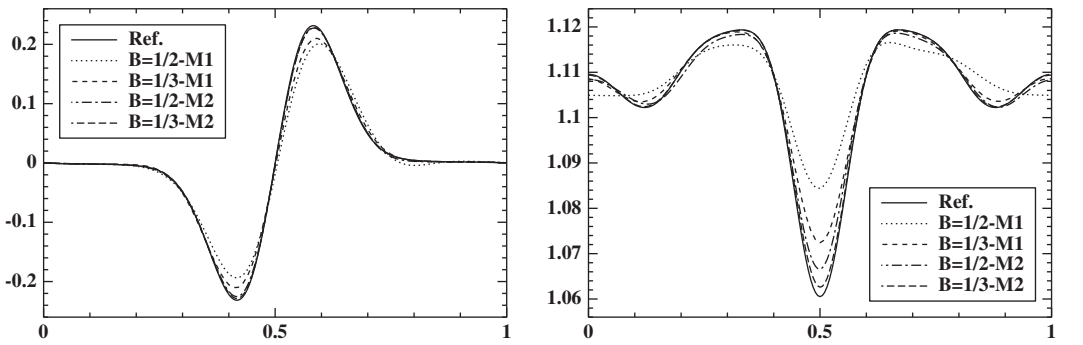

Figure 2. Non-dimensional profiles for vertical velocity (left) and pressure (right) along line $x_2 = \frac{1}{2}$ at time $t_5 = 5L/u_0$.

Table I. Relative errors (in %) for the maximum vertical velocity and the minimum pressure in the computational domain at times $t_i = iL/u_0$, $1 \leqslant i \leqslant 5$.

Max. vertical velocity	t_1	t_2	t_3	t_4	t_5
Reference value [9]	0.27855	0.26432	0.25060	0.24412	0.23163
$\beta = \frac{1}{2}$–mesh M1	−2.85	−4.97	−7.12	−9.32	−11.96
$\beta = \frac{1}{2}$–mesh M2	−0.06	−0.55	−0.82	−1.32	−1.78
$\beta = \frac{1}{3}$–mesh M1	−2.87	−4.53	−6.25	−8.01	−9.22
$\beta = \frac{1}{3}$–mesh M2	−0.33	−0.62	−0.93	−1.13	−1.25
Min. pressure	t_1	t_2	t_3	t_4	t_5
Reference value [9]	1.01276	1.01789	1.01964	1.08101	1.06052
$\beta = \frac{1}{2}$–mesh M1	0.60	1.24	1.45	0.55	2.08
$\beta = \frac{1}{2}$–mesh M2	0.06	0.22	0.31	−0.05	0.55
$\beta = \frac{1}{3}$–mesh M1	0.48	0.75	0.89	0.75	1.11
$\beta = \frac{1}{3}$–mesh M2	0.05	0.11	0.13	0.10	0.23

errors with respect to the benchmark solution for the maximum vertical velocity at non-dimensional time t_5 are respectively given by −0.78, −1.25, and −1.37%.

We now investigate the dissipative errors induced by the relaxation scheme. To this purpose, we consider a fictitious gas with $\gamma_1 = 1.66$. For the sake of brevity, we only discuss the simulations performed with $\beta = \frac{1}{3}$ on mesh M2. We compare the solutions obtained with and without relaxation but with the same Navier–Stokes solver so that the errors we report only contain the dissipative contribution of energy relaxation. Table II presents the relative errors

Table II. Relative errors (in %) for the maximum vertical velocity and the minimum pressure in the computational domain at times $t_i = iL/u_0$, $1 \leqslant i \leqslant 5$; comparison of the solutions obtained with relaxation ($\gamma_1 = 1.66$) and without relaxation.

Relative errors (%)	t_1	t_2	t_3	t_4	t_5
Max. vertical velocity	−0.003	−0.037	0.042	−0.127	−0.050
min. pressure	0.004	0.012	−0.025	−0.038	−0.033

for the maximum vertical velocity and the minimum pressure in the computational domain at times $t_i = iL/u_0$ with $1 \leqslant i \leqslant 5$. Dissipative errors induced by the relaxation method are seen to be at least an order of magnitude lower than discretization errors. These results demonstrate that vortex convection may be accurately predicted by the energy relaxation method.

4.2. *Temperature spot/weak shock interaction*

We consider a weak shock separating two uniform flows with the upstream one initially perturbed by a temperature spot. For this test problem, temperatures vary between 300 and 600 K. We assume that the real gas is TP and consider three models for its adiabatic exponent:

[C1] the real gas is actually TPCP with $\gamma = 1.4$;
[C2] $\gamma(T)$ is given as a second-order polynomial in the temperature

$$\gamma(T) = aT^2 + bT + c \tag{25}$$

with coefficients $a = -6.85\,10^{-8}\ \mathrm{K}^{-2}$, $b = -4.76\,10^{-6}\ \mathrm{K}^{-1}$ and $c = 1.3526$ obtained by fitting experimental values for air between 300 and 600 K;
[C3] $\gamma(T)$ follows a vibrational law in the form

$$\gamma(T) = 1 + \frac{1}{\frac{5}{2} - (\frac{T_v}{T})^2 \frac{\exp(T_v/T)}{(\exp(T_v/T)-1)^2}} \tag{26}$$

with the vibrational temperature set to $T_v = 1000$ K.

Figure 3 presents the adiabatic exponent as a function of temperature for the polynomial model (25) and the vibrational model (26).

Left and right states with respect to the shock are indexed, respectively, by L and R, both consisting of a uniform, horizontal flow. For the left state, the thermodynamic variables are given by $\rho_\mathrm{L} = 1.2\ \mathrm{kg\,m^{-3}}$, $T_\mathrm{L} = 300$ K, $p_\mathrm{L} = 103,320$ Pa, and the velocity vector by $U_\mathrm{L} = (u_\mathrm{L}, 0)$ where u_L is determined by setting the Mach number to $M = 1.1588$. The right state is then determined by solving the Rankine–Hugoniot conditions

$$\begin{aligned} \rho_\mathrm{L} u_\mathrm{L} &= \rho_\mathrm{R} u_\mathrm{R} \\ \rho_\mathrm{L} u_\mathrm{L}^2 + p_\mathrm{L} &= \rho_\mathrm{R} u_\mathrm{R}^2 + p_\mathrm{R} \\ h_\mathrm{L} + u_\mathrm{L}^2/2 &= h_\mathrm{R} + u_\mathrm{R}^2/2 \end{aligned} \tag{27}$$

where $h = \varepsilon + p/\rho$ is the specific enthalpy. Numerical values are given in Table III for the three thermodynamic models.

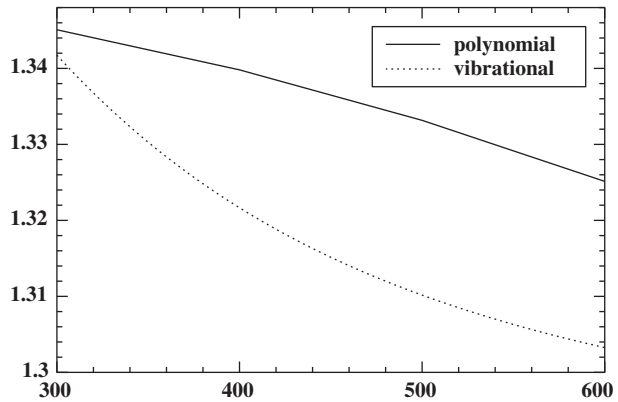

Figure 3. Adiabatic exponent as a function of temperature (K) for polynomial model (25) and vibrational model (26).

Table III. Test case 2: initial conditions for the three thermodynamic models.

Model	C1	C2	C3
u_L (m/s)	402.32	394.35	393.86
u_R (m/s)	316.71	308.33	307.23
ρ_R (kg m^{-3})	1.52	1.53	1.53
p_R (Pa)	144 648	144 022	144 263
T_R (K)	330.63	326.97	326.75

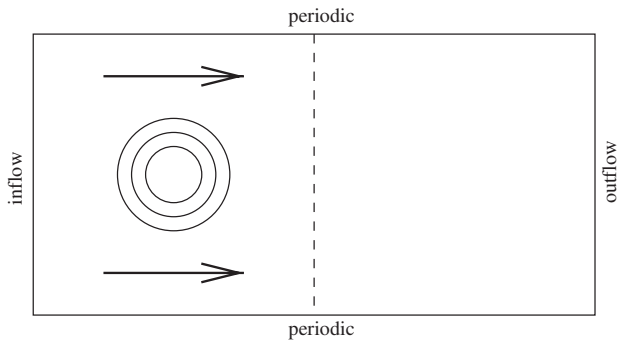

Figure 4. Initial flow configuration for test case 2.

The problem is posed on the domain $\Omega = [0, 2L] \times [0, L]$ where L is the reference length. The shear viscosity and the thermal conductivity are determined by setting the Reynolds number to $Re = 2000$ and the Prandtl number to $Pr = 0.7$, both numbers being evaluated using the left state as reference state and a reference length of $L = 1$ m. The initial flow configuration is depicted in Figure 4. Inflow and outflow conditions are imposed, respectively, on the left and right boundaries, whereas periodic conditions are considered for the bottom and top ones.

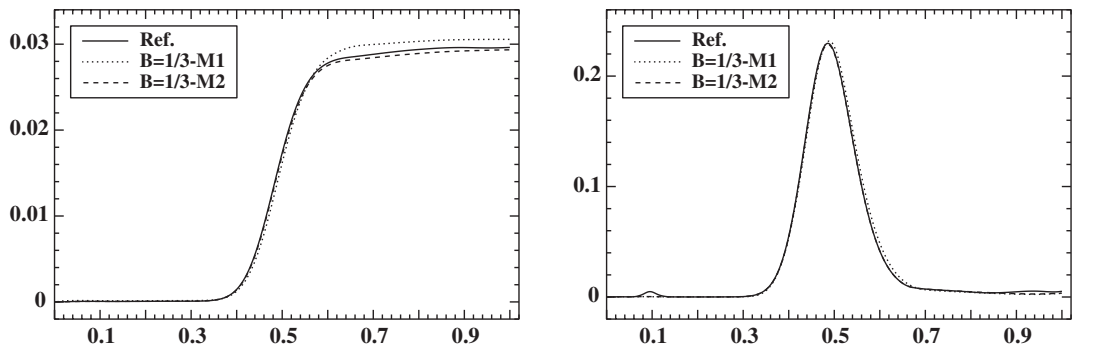

Figure 5. Time evolution of vorticity integral (left) and baroclinic torque (right) predicted by the reference solution and our TPCP Navier–Stokes solver on meshes M1 and M2.

The shock is located at non-dimensional co-ordinate $x = 1$. The temperature spot is initially centred at point $(\frac{1}{2}, \frac{1}{2})$ and is given in non-dimensional form by

$$\Delta T(x_1, x_2) = \frac{1}{c^4}(r^2 - c^2)^2 \mathrm{e}^{-r^2/\delta^2} \tag{28}$$

with $c = 7$, $\delta = 0.07$, and $r^2 = (x_1 - \frac{1}{2})^2 + (x_2 - \frac{1}{2})^2$. The temperature spot is convected by the base flow and starts interacting with the weak shock at non-dimensional time $t_* = (u_1/L)t \approx \frac{1}{2}$. The main physical process at play is the creation of vorticity through the baroclinic torque $-(1/\rho^2)\nabla p \times \nabla \rho$. Such process is important for instance when modelling turbulence creation inside a combustion chamber.

We first assess numerical errors in the absence of relaxation. We compare the results produced by our TPCP Navier–Stokes solver with the benchmark solution reported in Reference [9]. The latter was obtained using the time and space discretization described in the previous section on a uniform, quadrangular mesh containing 801×101 nodes. Our numerical results have been obtained using the β-scheme with $\beta = \frac{1}{3}$ on two triangulations constructed from a uniform, quadrangular mesh with cells split along alternating diagonals. The coarse one (mesh M1) contains 201×101 nodes and the fine one (mesh M2) contains as many nodes as the benchmark mesh. Figure 5 displays the time evolution of the integrals

$$\int_\Omega |\omega| \, \mathrm{d}\Omega \quad \text{and} \quad \int_\Omega \frac{1}{\rho^2} |\nabla p \times \nabla \rho| \, \mathrm{d}\Omega \tag{29}$$

where $\omega = \partial_1 u_2 - \partial_2 u_1$ is the vorticity and $U = (u_1, u_2)$ the two-dimensional velocity vector. No vorticity is initially present in the flow. Vorticity production through the baroclinic torque peaks at $t_* \approx 0.5$ when the centre of the vortex is located at the shock, and most of the vorticity has been generated at $t_* \approx 0.6$. Our numerical results compare very well with the reference solution, with those on the finer mesh yielding excellent agreement.

We have also compared our numerical solutions obtained on three types of meshes, all containing approximately the same number of nodes: two triangulations obtained by splitting either along alternate or uniform diagonals the cells of a uniform, quadrangular mesh and a fully unstructured Delaunay triangulation. Excellent agreement is achieved between the results obtained on the alternate mesh and the unstructured one. On the other hand, uniform cell

Table IV. Maximum vorticity at time t_2 obtained with the TPCP Navier–Stokes and the relaxation solvers on meshes M1 and M2; relative error (in %) with respect to the reference solution.

Scheme	Maximum of ω	Relative error
TPCP NS M1	0.97675	−6.58
TPCP Relax. M1	1.00475	−3.90
TPCP NS M2	1.01816	−2.62
TPCP Relax. M2	1.01647	−2.78

Table V. Relative error (in %) with respect to the reference solution for the vorticity integral at various non-dimensional times: TPCP Navier–Stokes solver (line 1) and relaxation method (line 2).

Non-dimensional time	0.25	0.5	0.75	1.0
TPCP NS (%)	−1.25	−1.35	−1.50	−0.97
Relaxation (%)	−2.44	−1.38	−1.65	−1.10

splitting leads to a much lower accuracy as far as vorticity production is concerned, with major discrepancies occurring before the temperature spot reaches the shock. Such meshes therefore require a much higher level of refinement to yield accuracies similar to the other types of meshes and will not be further considered.

We now investigate the accuracy and stability of the relaxation method. We first consider model C1 and set the adiabatic exponent of the fictitious gas to $\gamma_1 = 1.66$ in agreement with the subcharacteristic condition (11). Figure 6 presents density and vorticity isocontours for non-dimensional times $t_1 = \frac{1}{2}$ and $t_2 = 1$ as predicted by the relaxation method and the TPCP Navier–Stokes solver on mesh M2. Excellent agreement is achieved. Table IV presents the values of the maximum vorticity at time t_2 for the two methods on the two meshes as well as the relative error (in %) with respect to the reference solution. On the finer mesh, the results are quite satisfactory and show in particular that the error due to the relaxation method is much smaller than that due to discretization. On the coarse mesh, the error due to discretization is too large to assess the error due to relaxation. Table V presents relative errors (in %) on the vorticity integral at non-dimensional times $t_* = 0.25$, 0.5, 0.75, and 1. Errors between the TPCP Navier–Stokes solver and the reference solution are very close to those obtained with the relaxation method, confirming that the dissipative errors induced by energy relaxation are much smaller than those induced by the discretization. Despite the presence of some vorticity in the shock at time t_2, both the Navier–Stokes solver and the relaxation method slightly underestimate the total vorticity. This results from the fact that in both cases, slightly lower values for the maximum vorticity are obtained.

We next consider the thermodynamic models C2 and C3 in which the adiabatic exponent is a non-linear function of the temperature. The adiabatic exponent of the fictitious gas is set to $\gamma_1 = 1.38$ in agreement with the subcharacteristic condition (11) (see Figure 3). We compare our numerical results with those obtained from an extended Navier–Stokes code in which the Riemann solver is modified to account for the temperature dependency of the adiabatic exponent, i.e. in which the Jacobian matrices associated with convective fluxes are modified to include the correct values of pressure derivatives. In the Roe scheme, the mean

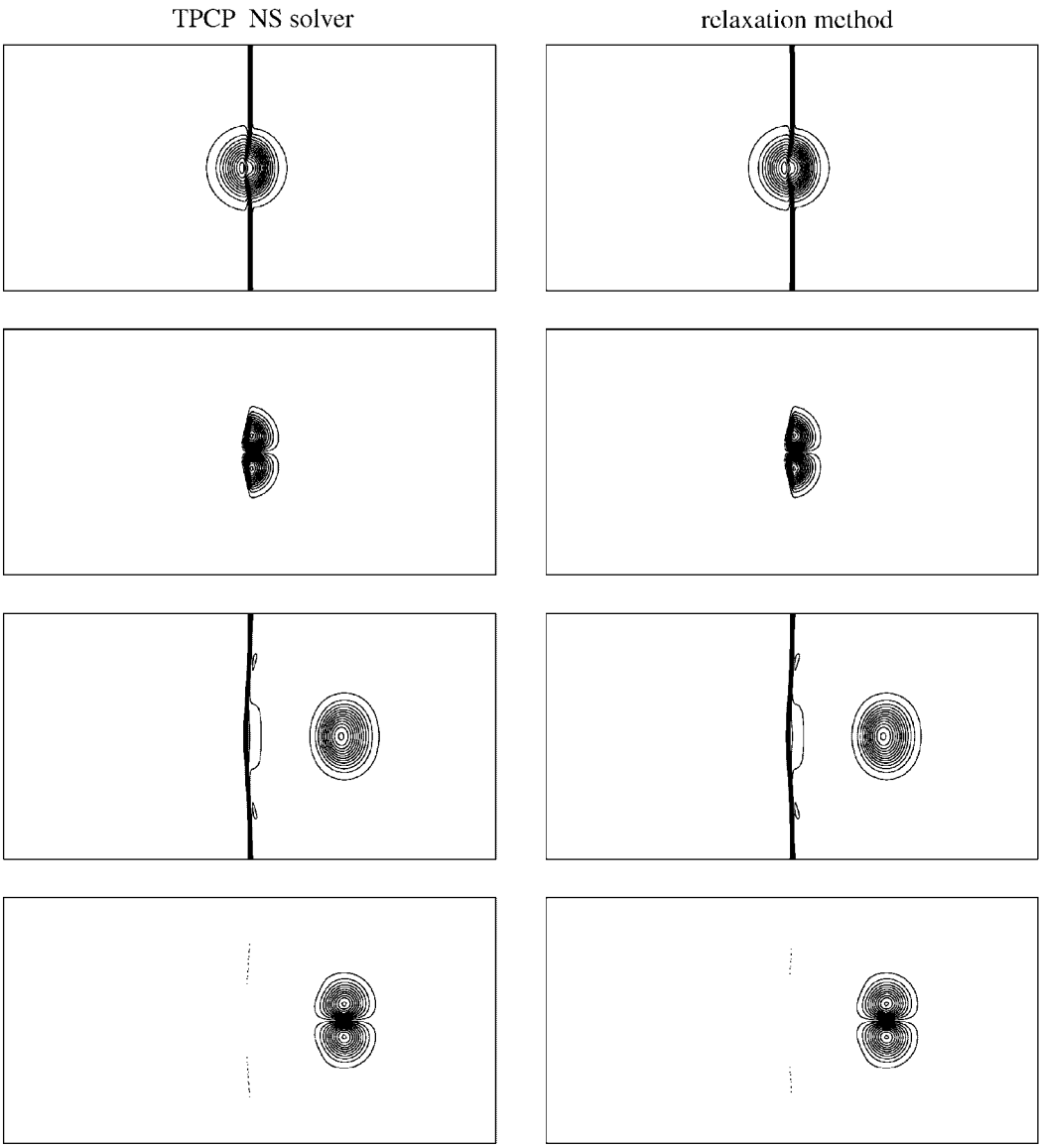

Figure 6. Comparison of density and vorticity isocontours as predicted by the TPCP Navier–Stokes solver (left column) and the relaxation method (right column): ρ at time t_1 (top line); ω at time t_1 (second line); ρ at time t_2 (third line); ω at time t_2 (bottom line.)

values of these matrices then depend on mean values of the temperature and the adiabatic exponent. Figure 7 displays density profiles along line $x_2 = \frac{1}{2}$ for non-dimensional times $t_1 = \frac{1}{2}$ and $t_2 = 1$ obtained on meshes M1 and M2 for thermodynamic model C2. Excellent agreement between the energy relaxation method and the extended Navier–Stokes solver is obtained on

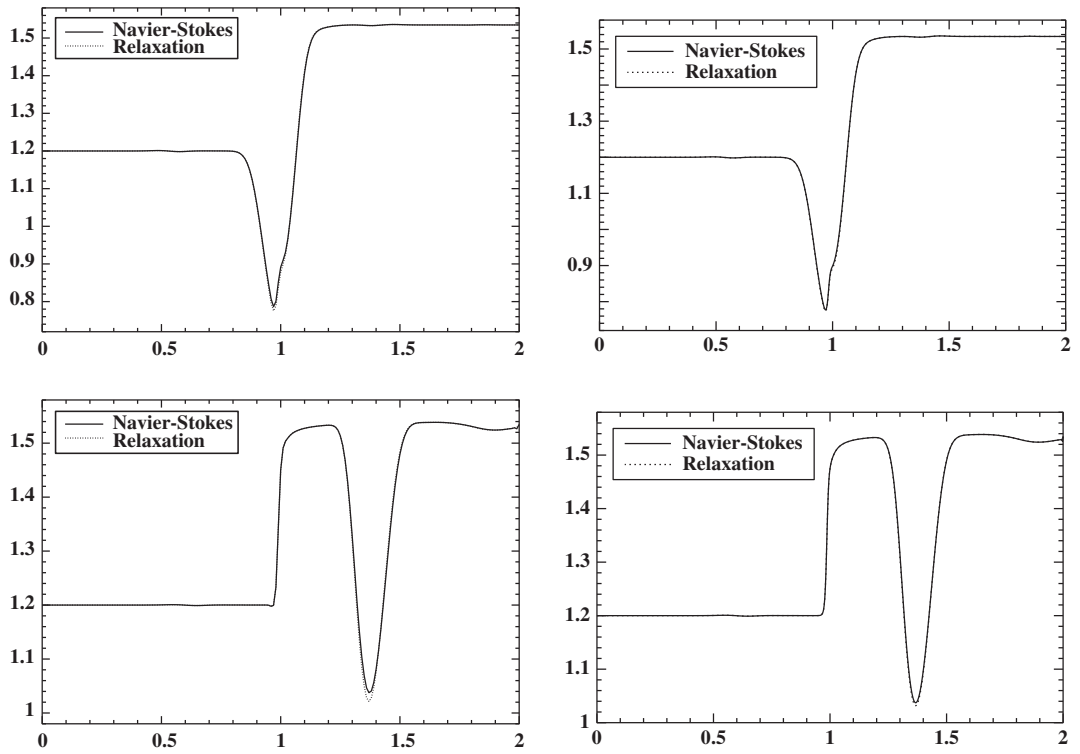

Figure 7. Density profiles along line $x_2 = \frac{1}{2}$ for non-dimensional times $t_1 = \frac{1}{2}$ (top) and $t_2 = 1$ (bottom) predicted by the extended Navier–Stokes solver and the relaxation method. Thermodynamic model C2. Left: mesh M1. Right: mesh M2.

Table VI. CPU times obtained with the relaxation method normalized by those obtained with the extended Navier–Stokes solver.

Time step	CFL = 1.5		$\Delta t = 0.15 \times 10^{-5}$	
Model	C2	C3	C2	C3
Relative CPU	1.14	1.04	1.21	1.09

both meshes, with minor differences (of the order of a few percent) only occurring at the core of the temperature spot. Similar results are obtained for model C3. These results confirm the ability of the energy relaxation method to predict accurately the dynamics of non-isothermal flows with moderate temperature gradients.

We conclude this section with a brief assessment of computational times. Table VI reports CPU times obtained with the energy relaxation method normalized by those obtained with the extended Navier–Stokes code. Computations are performed for the β-scheme with $\beta = \frac{1}{3}$ on mesh M2. We consider the real gas models C2 and C3. In the first two columns of Table VI, the time step is adjusted adaptively based on a CFL condition. Since the

relaxation method uses the (higher) sound speed of the fictitious gas, this yields a more stringent CFL condition for the energy relaxation method and thus a larger number of time steps. A second set of comparisons is performed by keeping the time step constant at the value of $\Delta t = 0.15 \times 10^{-5}$. Both sets of comparisons yield similar results. The overhead incurred by the relaxation method ranges between 10 and 20% for the polynomial model C2 and between 4 and 9% for the vibrational model C3. The computational overhead is less important for the latter model because the extended convective flux solver is more expensive. Indeed, in model C3, the energy law $\varepsilon := \varepsilon(T)$ cannot be explicitly inverted, requiring an iterative procedure each time a temperature is evaluated. Although the convergence rate is extremely fast (one or two iterations typically), this suffices to impact the cost of the extended Navier–Stokes code.

4.3. Reflected shock/boundary layer interaction

We consider a square shock tube with insulated walls and unit side length. A diaphragm is located in the middle of the tube ($x_1 = 0.5$), separating two uniform states indexed by L (left state) and R (right state). The right state corresponds to air at standard thermodynamic conditions. The left state is given by $\rho_L/\rho_R = p_L/p_R = 100$ and $T_L = T_R$. To begin with, we assume that the gas inside the shock tube is TPCP with $\gamma = 1.4$. The shear viscosity and the thermal conductivity are evaluated from a Reynolds number of either 200 or 1000 and a Prandtl number of 0.7. It is worthwhile to point out that this test case is strongly non-isothermal with temperatures ranging from 300 K up to 2000 K.

At the initial time, the diaphragm is broken. In the inviscid case, a shock wave with Mach number 2.37 moves to the right and is followed by a contact discontinuity. At non-dimensional time $t_* \approx 0.2$, the shock wave is reflected at the right wall and interacts with the contact discontinuity, yielding complex flow dynamics. The contact discontinuity stays stationary in the vicinity of the right wall. The reflected shock starts interacting with the trailing rarefaction wave centred at $x_1 = 0.5$ at non-dimensional time $t_* \approx 0.4$. In the viscous case, the shock wave and the contact discontinuity generate a thin boundary layer in the vicinity of the horizontal wall of the tube as they propagate to the right. After being reflected, the shock wave interacts with the boundary layer yielding complex flow patterns with vortex generation. A more thorough discussion of physical aspects is given in Reference [10]. For $Re = 200$, reference solutions have been obtained in Reference [10] and more recently in Reference [18]. For $Re = 1000$, it is not certain that the flow is stable, but the test case is of interest to compare our results with those presented in References [10, 18].

Owing to the symmetry with respect to the line located at $x_2 = 0.5$, we reduce the computational domain to $\Omega = (0, 1) \times (0, 0.5)$. Symmetry conditions are enforced on the top boundary while no-slip, adiabatic conditions are enforced elsewhere. We consider three triangulations obtained by splitting along alternate diagonals the cells of uniform, quadrangular meshes. The coarsest mesh (mesh M1) contains 501×251 nodes, the middle one (mesh M2) 1001×501 nodes, and the finest one (mesh M3) 1501×751 nodes. Meshes M1 and M2 are used for the $Re = 200$ computations and meshes M2 and M3 for the $Re = 1000$ computations. We consider the two high-order limiter functions described in Section 3 [14] and yielding third- and fourth-order accuracy, at least away from discontinuities. The CFL is linearly increased in time from an initial value of 0.2 up to 1.5. We first discuss our results for $Re = 200$ and then for $Re = 1000$.

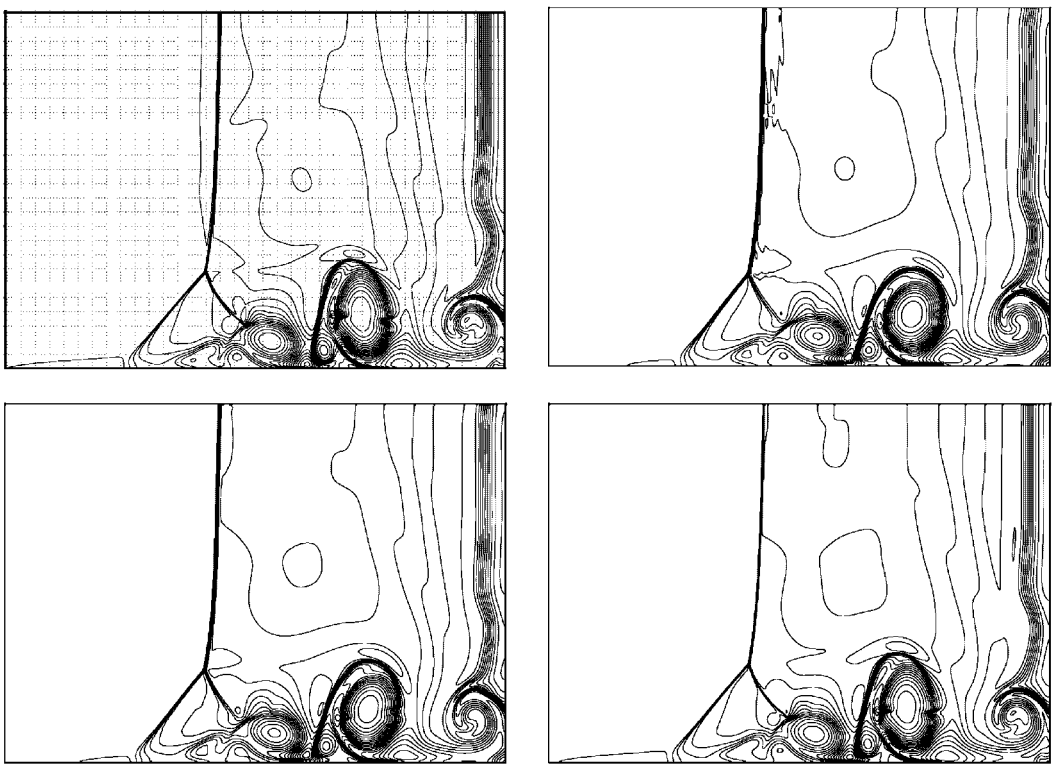

Figure 8. Density isocontours at non-dimensional time $t_* = 1$ for $Re = 200$. Top, left: reference solution. Top, right: third-order limiter on mesh M1. Bottom, left: fourth-order limiter on mesh M1. Bottom, right: fourth-order limiter on mesh M2. The plotting domain is $(0.3, 1) \times (0, 0.4)$.

For $Re = 200$, we use as a reference solution the one obtained in Reference [10] with a third-order Runge–Kutta method for time integration, a second-order TVD scheme for spatial discretization [19], the Van Leer harmonic limiter function, and a uniform, quadrangular mesh containing 1000×500 nodes. Other numerical schemes are also investigated in Reference [10], which are equivalent for our validation purposes. Figure 8 presents isocontours for the density at non-dimensional time $t_* = 1$ obtained with the two limiter functions and meshes M1 and M2. A comparison with the benchmark solution shows that in all cases the key features of the flow dynamics generated by the interaction of the shock wave and the boundary layer are captured. Large vortices are generated in the boundary layer bubble resulting from the pressure difference between the stagnation pressure in the boundary layer and that of the outflow region. The third-order limiter function yields spurious oscillations behind the shock wave. Such oscillations are wiped out by the fourth-order limiter function. Independently from the limiter function, we also observe that for mesh M1, the main vortex behind the λ-shaped shock wave is slightly more bent to the right whereas for mesh M2, the calculations agree well with the reference solution.

Turning to the accuracy and stability of the relaxation method, we first consider the case where the real gas is still TPCP, and the fictitious gas is also TPCP with $\gamma_1 = 1.66$. In

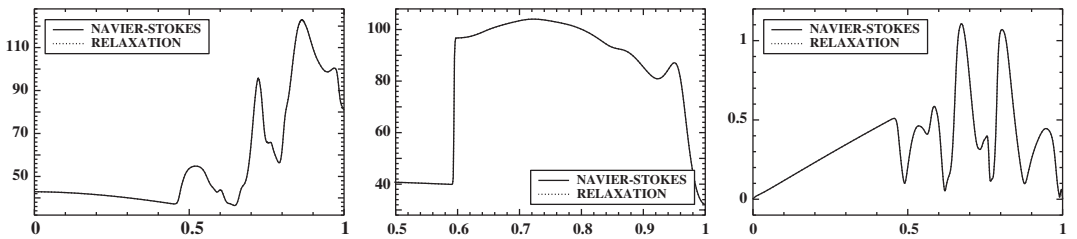

Figure 9. Density and Mach number profiles at non-dimensional time $t_* = 1$ for $Re = 200$ predicted by the TPCP Navier–Stokes solver and the energy relaxation method on mesh M2: density along line $x_2 = 0$ (left); density along line $x_2 = 0.3$ (middle); Mach number along line $x_2 = 0.01$ (right.)

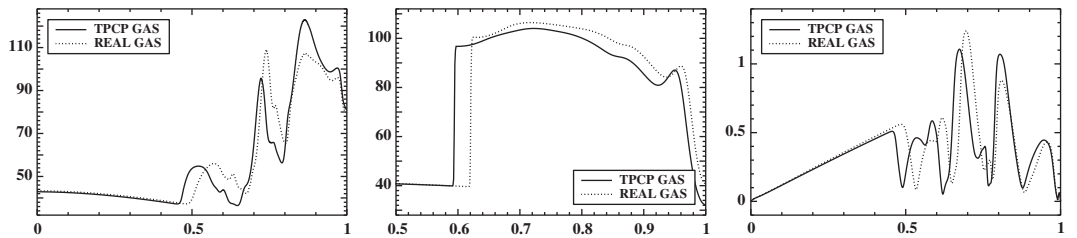

Figure 10. Density and Mach number profiles at non-dimensional time $t_* = 1$ for $Re = 200$ obtained with the TPCP gas model and the vibrational model on mesh M2 (the same non-dimensionalization is used for both calculations): density along line $x_2 = 0$ (left); density along line $x_2 = 0.3$ (middle); Mach number along line $x_2 = 0.01$ (right.)

order to minimize discretization errors, comparisons are made with the solutions predicted on mesh M2 with the fourth-order limiter function. Figure 9 presents density and Mach number profiles along various horizontal lines at non-dimensional time $t_* = 1$. Profiles obtained with and without relaxation overlap, confirming the accuracy of the relaxation method.

We next investigate the case where the adiabatic exponent is temperature dependent and follows the vibrational model (26). Because of the strong temperature variations present in the flow, non-linearities arising in the adiabatic exponent yield a sizeable impact on the flow dynamics. Vibrational effects mainly result from the dependency of the sound speed on the adiabatic exponent and are illustrated in Figure 10 where density and Mach number profiles are presented at non-dimensional time $t_* = 1$. Numerical results are obtained with the extended Navier–Stokes code. Vibrational effects have a strong impact on the flow temperature which now varies between 425 and 1676 K. Turning to the accuracy and stability of the energy relaxation method for gas flows with vibrational effects, we compare the results obtained with the extended Navier–Stokes code to those delivered by the relaxation method. Figure 11 presents density and Mach number profiles at non-dimensional time $t_* = 1$. The agreement appears to be excellent. The relaxation method thus captures the correct flow dynamics although the fictitious gas alone would yield significantly different flow patterns. The accuracy of the relaxation method is further confirmed in Figure 12 which presents density isocontours at non-dimensional time $t_* = 1$. Note that the shape of the main vortex is significantly different from that obtained with the TPCP gas model (Figure 8).

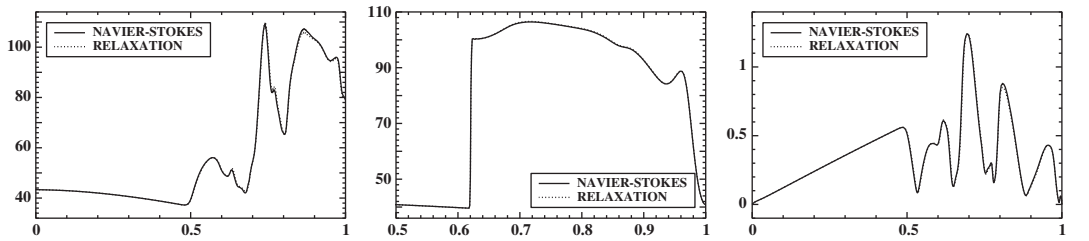

Figure 11. Density and Mach number profiles at non-dimensional time $t_* = 1$ for $Re = 200$ obtained on mesh M2 for the vibrational model C3 using the energy relaxation method and the extended Navier–Stokes solver: density along line $x_2 = 0$ (left); density along line $x_2 = 0.3$ (middle); Mach number along line $x_2 = 0.01$ (right.)

Figure 12. Density isocontours for vibrational model C3 at non-dimensional time $t_* = 1$ for $Re = 200$ obtained on mesh M2 with the extended Navier–Stokes code (left) and the energy relaxation method (right); plotting domain as in Figure 8.

Finally, we investigate the case $Re = 1000$. For such Reynolds number, vortical structures become extremely complex. Small vortices are generated just downstream of the boundary layer separation, and shocklets are present at many locations inside the large vortices. Figure 13 presents density isocontours at non-dimensional time $t_* = 1$ predicted for a TPCP gas on mesh M3 with and without relaxation. The flow patterns are extremely close, confirming that also at high Reynolds numbers, the errors induced by the relaxation method are marginal with respect to those caused by discretization. Our results also agree reasonably well with those reported by Daru and Tenaud [10] using a 2000×1000 mesh and those of Sjögreen and Yee [18] using a 4000×2000 mesh. Except for some fine scale vortices (e.g. those located in the layer at $x_1 = 0.9$), the global structure of the flow is well represented. More importantly for our purposes, the errors induced by the relaxation method do not come into play. This conclusion is further confirmed in Figure 14 where density profiles along the bottom wall at non-dimensional time $t_* = 1$ are presented. Grid resolution clearly has an impact on the profiles, while the energy relaxation method does not yield any significant error.

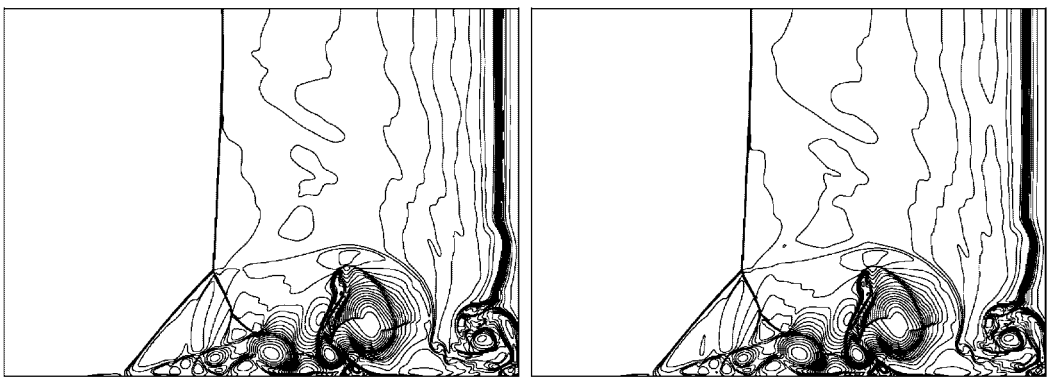

Figure 13. Density isocontours for a TPCP gas at non-dimensional time $t_* = 1$ for $Re = 1000$ obtained on mesh M3 with the TPCP Navier–Stokes code (left) and the energy relaxation method (right); plotting domain as in Figure 8.

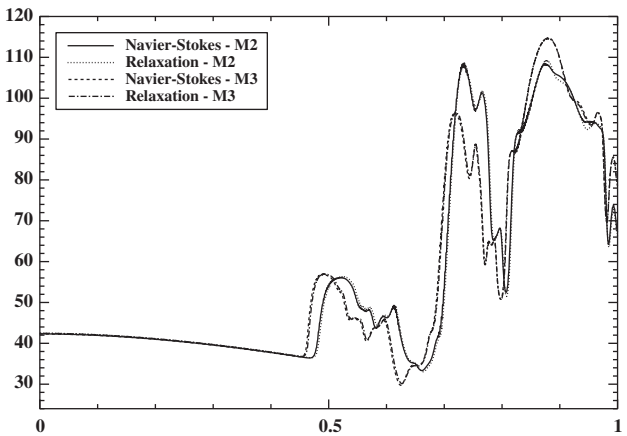

Figure 14. Density profiles along bottom wall at non-dimensional time $t_* = 1$ for $Re = 1000$ obtained on mesh M3 with the TPCP Navier–Stokes code and the energy relaxation method.

5. CONCLUSIONS

In this paper, we have evaluated numerically a new energy relaxation method for the simulation of unsteady, viscous, thermically perfect but calorifically imperfect gas flows governed by the compressible Navier–Stokes equations. We have investigated three test problems of increasing difficulty: the isothermal advection of a periodic set of vortices in order to assess the basic dissipative errors, the interaction of a temperature spot with a weak shock in order to validate the splitting of the heat flux vector in a test case where non-linearities in the adiabatic exponent have a moderate impact on the flow dynamics, and finally, the interaction of a reflected shock with its trailing boundary layer in order to assess the capability of the energy relaxation method to tackle complex flow dynamics. Our results have been compared

to benchmark solutions and numerical errors due to both discretization and energy relaxation have been assessed independently. In all cases, the energy relaxation method is able to predict accurately the flow dynamics, while inducing only marginal overheads in computational times. Future work includes the evaluation of the energy relaxation method on wall heat transfer problems and on gas flows governed by thermodynamic models that involve additional non-linearities with respect to the TP gas model.

ACKNOWLEDGEMENTS

The authors are grateful to Dr C. Tenaud for stimulating scientific discussions and for providing the data of the reference solutions.

REFERENCES

1. Anderson Jr. JD. *Hypersonic and High Temperature Gas Dynamics*. McGraw-Hill: New York, 1989.
2. Colella P, Glaz HM. Efficient solution algorithm for the Riemann problem for real gases. *Journal of Computational Physics* 1985; **59**:264–289.
3. Glaister P. An approximate linearized Riemann solver for the Euler equations for real gases. *Journal of Computational Physics* 1988; **74**:382–408.
4. Abgrall R. Extension of Roe's approximate Riemann solver to equilibrium and non-equilibrium flows. In Wesseling P (ed.), *Notes on Numerical Fluid Mechanics*, vol. 29. Vieweg: Braunschweig, 1990:1–10.
5. Liu TP. Hyperbolic conservation laws with relaxation. *Communications in Mathematical Physics* 1987; **108**:153–175.
6. Chen GQ, Levermore CD, Liu TP. Hyperbolic conservation laws with stiff relaxation terms and entropy. *Communications in Pure and Applied Mathematics* 1994; **47**:787–830.
7. Coquel F, Perthame B. Relaxation of energy and approximate Riemann solvers for general pressure laws in fluid dynamics. *SIAM Journal on Numerical Analysis* 1998; **35**:2223–2249.
8. Bongiovanni E, Ern A, Glinsky-Olivier N. A new relaxation method for the compressible Navier–Stokes equations. *Mathematical Models and Methods in Applied Science* 2003; **13**:1379–1396.
9. Tenaud C, Garnier E, Sagaut P. Evaluation of some high-order shock capturing schemes for direct numerical simulation of unsteady two-dimensional free flows. *International Journal for Numerical Methods in Fluids* 2000; **33**:249–278.
10. Daru V, Tenaud C. Evaluation of TVD high resolution schemes for unsteady viscous shocked flows. *Computers and Fluids* 2001; **30**:89–113.
11. In A. Numerical evaluation of an energy relaxation method for inviscid real fluids. *SIAM Journal on Scientific Computing* 1999; **21**(1):340–365.
12. Montarnal P, Shu CW. Real gas computation using an energy relaxation method and high-order WENO schemes. *Journal of Computational Physics* 1999; **148**:59–80.
13. Désideri JA, Goudjo A, Selmin V. Third-order numerical schemes for hyperbolic problems. *INRIA Research Report* 607, 1987.
14. Piperno S, Depeyre S. Criteria for the design of limiters yielding efficient high resolution TVD schemes. *Computational Fluids* 1998; **27**:183–197.
15. Larrouturou B. How to preserve mass fraction positivity when computing compressible multi-component flows. *Journal of Computational Physics* 1991; **95**:59–84.
16. Fézoui L, Lantéri S, Larrouturou B, Olivier C. Résolution numérique des équations de Navier–Stokes pour un fluide compressible en maillage triangulaire. *INRIA Research Report* 1033, 1989.
17. Steger J, Warming RF. Flux vector splitting for the inviscid gas dynamic with applications to finite difference methods. *Journal of Computational Physics* 1981; **40**:263–293.
18. Sjögreen B, Yee HC. Grid convergence of high order methods for multiscale complex unsteady viscous compressible flows. *Journal of Computational Physics* 2003; **185**:1–26.
19. Yee HC, Harten A. Implicit TVD schemes for hyperbolic conservation laws in curvilinear co-ordinates. *AIAA Journal* 1987; **25**:266–274.

